Technische Universität München
Fakultät für Physik

Bachelor thesis in physics

Study of propagating discharges in GEM-based detectors

Untersuchungen zu propagierenden Entladungen in GEM-basierten Detektoren

Florian Dufter

August 26th 2016

Excellence Cluster
Universe

Primary reviewer: Prof. Dr. Laura Fabbietti
Secondary reviewer: Prof. Dr. Peter Fierlinger
Supervisor: M. Sc. Andreas Mathis

Contents

Introduction

The LHC[1], located at the CERN[2] facility in Switzerland, collides protons and ions at unprecedented center-of-mass energies of up to $\sqrt{s} = 13\,\mathrm{TeV}$ in pp and $\sqrt{s_{\mathrm{NN}}} = 5.02\,\mathrm{TeV}$ in Pb–Pb mode. ALICE[3] is an experiment dedicated to the study of the physics of strongly interacting matter and in particular to investigate the properties of the phase of deconfined matter, the so-called Quark-Gluon Plasma. The QGP is believed to have existed during the first millisecond after the big bang before the quarks started to hadronize and occurs after a phase transition from the hadronic phase at high temperatures and/or densities [1]. A thorough study of it may contribute to our understanding of the evolution of the universe and the physics of the strong interaction in general. ALICE with its multiple sub-detectors and excellent particle identification capabilities is a suitable tool to observe the particle output of ultra relativistic heavy-ion collisions. The TPC[4] is one of those sub-detectors and the main detector for momentum measurement and charged-particle tracking and identification in the central barrel of the ALICE experiment. Currently, the readout is conducted with MWPCs[5], which employ a so-called gating grid to prevent the ions created in the amplification process from drifting back into the active volume, where they would cause field distortions and thus a deterioration of the spatial resolution. The gating grid imposes an intrinsic rate limitation of 3.5 kHz, which complied with the requirements of the LHC RUN 1 and 2. However, in the course of the LHC luminosity upgrade, the interaction rate will be raised to 50 kHz from 2020 on. Thus, the MWPC-based readout has to be replaced with a GEM[6]-based one. The GEM's intrinsic IBF[7] suppression allows a continuous operation [2]. However, it is believed that high charge densities contained in single GEM holes may lead to electric discharges. Discharges severely disturb the operation of a GEM-based detector as they introduce inefficiencies and, moreover, may cause irreversible damage to the GEM, ranging from enhanced leakage currents to permanent electric short circuits that render the detector effectively blind and lead to a loss in acceptance. A further complication is that discharges may propagate through subsequent GEM foils in a

[1]Large Hadron Collider
[2]Organisation européenne pour la recherche nucléaire
[3]A Large Ion Collider Experiment
[4]Time Projection Chamber
[5]Multi Wire Proportional Chamber
[6]Gas Electron Multiplier
[7]Ion back flow

stack or from the last GEM and the readout anode. In particular the latter poses a severe threat to the front end electronics as such high currents may be destructive. The occurrence of those propagations is still not fully understood. Therefore, a thorough investigation of this phenomenon, as carried out in the course of this thesis, is essential to assure a stable and safe operation.

Chapter 1

GEM TPC

The TPC is the main tracking and particle identification device of the ALICE experiment. The MWPC-based readout will be replaced by a GEM-based one in the course of the LHC upgrade in order to record events at a higher interaction rate. However, discharges due to high charge densities contained in single GEM holes may occur as GEMs operate at harsh conditions. Secondary discharges, that follow the initial ones, are characterized by a larger amplitude and might be related to the propagation. They pose a significant threat to the GEM structure and the readout.

1.1 Time Projection Chamber

A TPC [3] is typically a cylindrical volume filled with a counting gas, which is usually a mixture of 90% noble gas and 10% quencher. The high voltage cathode is typically located in the center of the active volume with the readout anodes being at ground potential on the end plates, but other configurations are also possible as shown in Fig. 1.1. A potential is applied to the cathode, which creates an electric drift field parallel to the rotational axis of the TPC. To ensure homogeneity of the electric field, the volume is enclosed by a field-cage, consisting of several conducting strips, which lower the potential step-wise from the cathode to the anode. The particles emerging from the initial beam-beam interaction, which typically takes place in the middle of the TPC, create electron-ion pairs along their trajectory. The electrons drift along the electric field lines towards the anode of the TPC, while the ions move to the high voltage cathode. As the amount of created electron-ion pairs is only $\mathcal{O}(10)$ per centimeter for MIPs[1], the electrons have to be amplified to obtain a perceivable signal for the front end electronics. Typically, this is achieved with MWPCs [5], which consist of a cathode and an anode wire plane located in parallel above the padplane. By applying high voltage to the wires, strong electric fields emerge radially, therefore main amplification takes place in the closest vicinity of the wire. Figure 1.2 depicts a simulation of the electric field of a MWPC, with the color code giving information about the potential. Electrons entering the zone close

[1] Minimum Ionizing Particle

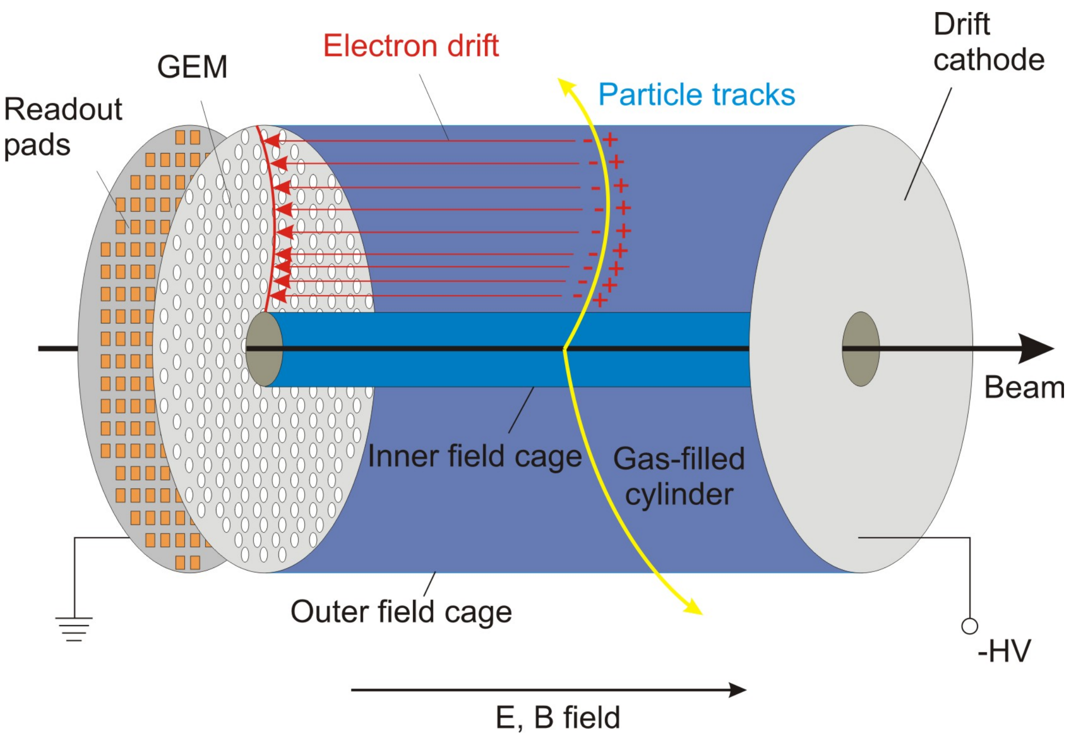

Figure 1.1: Schematic view of a TPC with GEM-based readout [4].

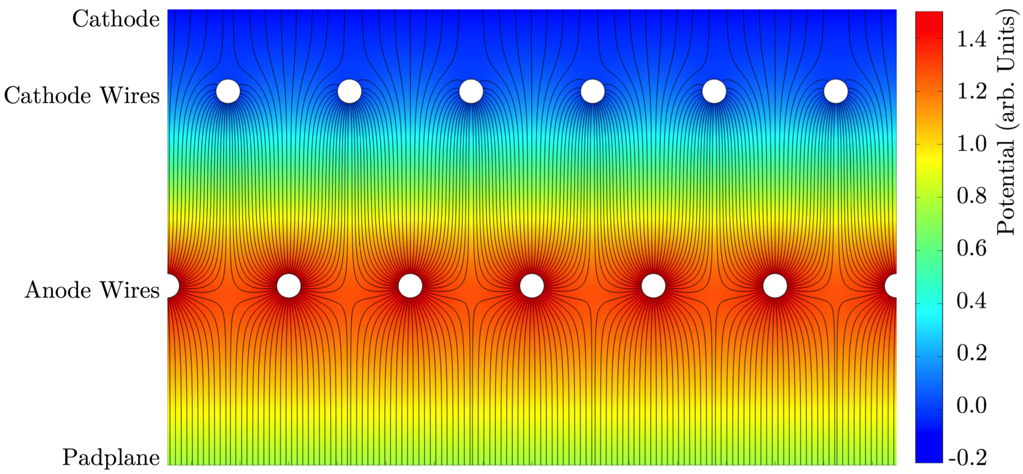

Figure 1.2: Simulated field configuration in a MWPC. The color represents the potential. Field lines are indicated in black [6].

to the anode wires are accelerated in the strong electric fields and eventually gain sufficient energy for further gas ionization. This leads to an avalanche of electrons, which then drift towards the anode wire, where they are neutralized and don't further contribute to the signal creation. However, positively charged ions are also created in this process. Due to their higher mass, they are much slower and thus more likely to follow the field lines back to the cathode wires or the readout. While drifting, they are inducing mirror charges in the padplane. The resulting signal is then recognized by the readout electronics.
Most ions are neutralized at the cathode wires. However, a significant amount of ions can propagate into the active volume. Due to their low drift velocity, the ions accumulate in the active volume and distort the drift field. Consequently, the drift path projection of the created electrons is severely altered. For proper reconstruction of the trajectories of the initial particles, this modification has to be corrected on by employing sophisticated calibration methods [7].
In order to circumvent this problem, the ions are blocked by a third wire plane. This so-called gating grid is located between the active volume and the cathode wire plane. In its open-configuration, the gating grid is transparent for incoming electrons from the drift region and ions stemming from the amplification region. After the amplification process, the potential of the gating grid is adjusted, so that positive ions are attracted. The ions drift to the grid, where they are neutralized. However, during this stage the detector is effectively rendered blind, as all incoming charge is blocked at the gating grid. Afterwards, the gating grid is opened again and the process is repeated. The gating grid suppresses the ion backflow to $\sim \mathcal{O}(10^{-5})$ [3].
The x- and y-coordinates are given by the projection of the track onto the readout plane. The z-coordinate is calculated from the drift time (time between collision and electrons arriving onto the readout pad) of the electrons in the gas. The starting time of the drift is obtained from external detectors. Typically, the TPC is placed in a magnetic field, which bends the trajectories of charged particles in the gas. The reconstruction of the momentum from the curvature of the trajectories along with the measurement of the specific energy loss ($\mathrm{d}E/\mathrm{d}x$) provides full PID[2].

1.2 Quark Gluon Plasma & the strong interaction

The quark-gluon plasma is a state, in which quarks are deconfined. It is believed to emerge after a phase transition at high temperatures and/or densities. A sketch of the QCD[3] phase diagram is shown in Fig. 1.3. Normal hadronic matter is found at low temperatures and baryon densities. Due to the color confinement, quarks

[2]Particle Identification
[3]Quantum Chromodynamics, the theory of the strong interaction

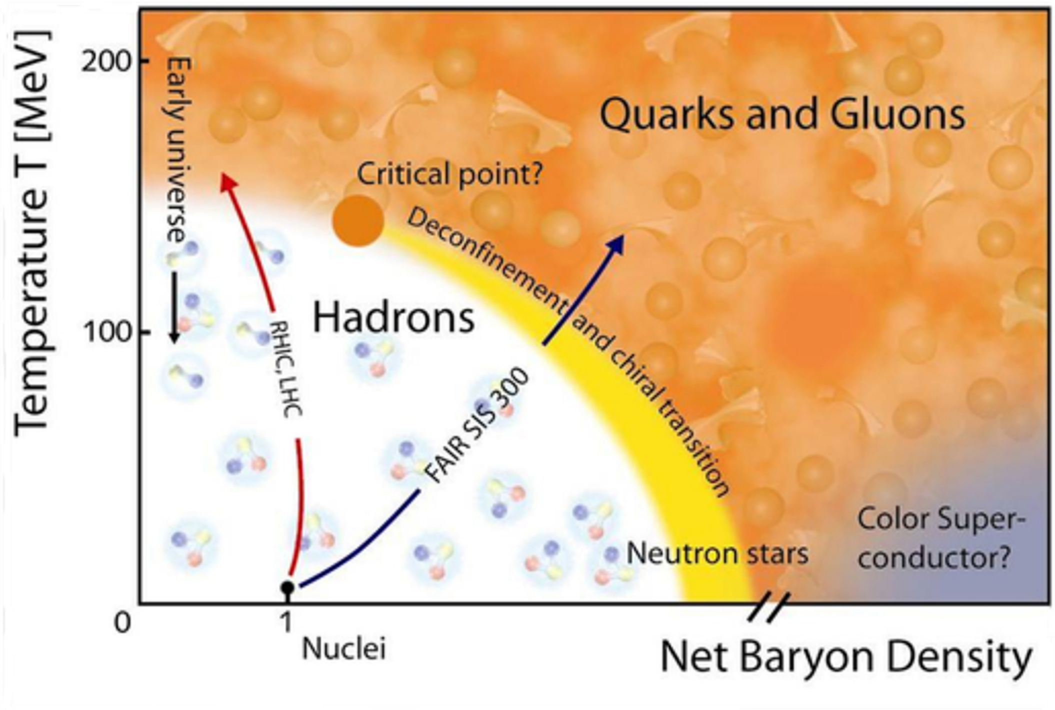

Figure 1.3: A sketch of the QCD phase diagram [8].

are bound in baryons and mesons. At high temperatures and/or high densities it is believed, that there is a phase transition of the bound quarks to a deconfined state. In this limit the quarks are assumed to be free. This transition is indicated in Fig. 1.3 by the yellow band. Large accelerators like the RHIC or the LHC try to create these conditions in ultrarelativistic heavy ion collisions. High densities and temperatures are created in the overlap region of two colliding nuclei and finally, the conditions for deconfinement might be fulfilled and the QGP emerges. Following that, the plasma expands adiabatically and cools down. When the plasma is cold enough, it transitions back in the hadronic phase and the quarks are rebound in hadrons. The reconstruction of those particles gives information about the conditions in the plasma. Additionally, there is also a production of photons from the plasma. This electromagnetic radiation does not cool down, because the interaction of the photons with the medium is reduced, and therefore provides information about the temperature and the conditions of the initial stage of the collision. However, the direct observation of those photons is rather difficult as these probes are emitted during the whole evolution of the collision system. Therefore, only the integrate photonic outcome can be studied.

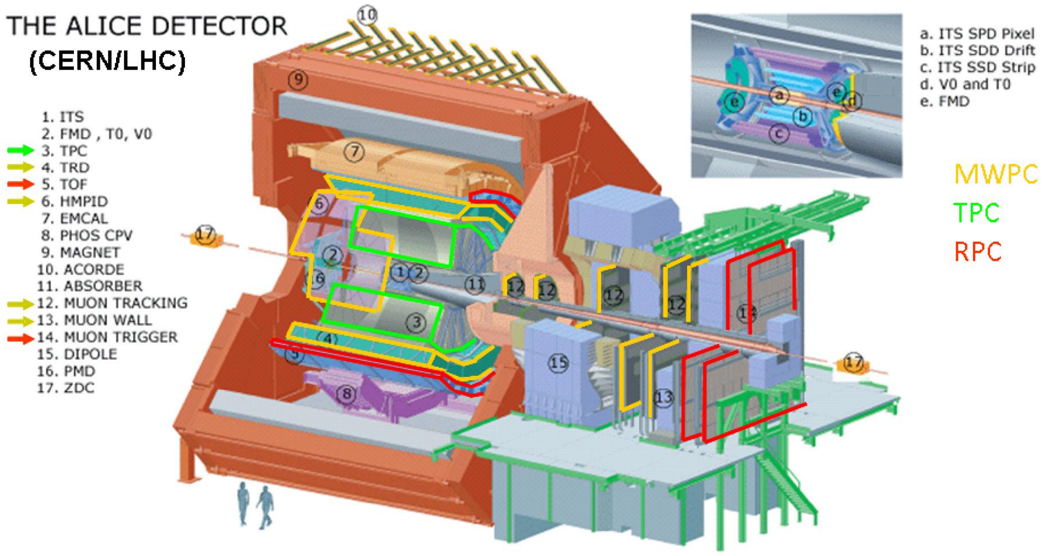

Figure 1.4: Schematic of the ALICE detector. Indicated are the gaseous-detectors. The insert shows the ITS [10].

The observation of the QGP is especially interesting due to the fact, that conditions similar to those, which existed in the early universe, can be created with it [9]. Therefore, the investigation of the QGP should give an insight of the processes that took place in the early universe.

1.3 ALICE – A Large Ion Collider Experiment

ALICE [2] is a heavy-ion-collider experiment at the LHC. It observes pp collisions at $\sqrt{s} = 13\,\text{TeV}$ and Pb–Pb collision at $\sqrt{s_{\text{NN}}} = 5.02\,\text{TeV}$ and is dedicated to study the physics of strong interaction. ALICE consists of multiple sub-detectors to observe the beam-beam interaction. The interaction vertex and low-momentum particles are detected by the ITS[4], a six-layer silicon detector. The ALICE TPC is the largest detectors of its type, being a cylindrically shaped vessel with a radius of 2.5 m and a length of 5 m, with a volume of around $90\,\text{m}^3$. The TPC acceptance covers 2π in azimuthal angle and a pseudo-rapidity interval of $|\eta| < 0.9$. It has the capability to deal with event multiplicities of up to $\mathrm{d}N_{\text{ch}}/\mathrm{d}\eta = 8000$ at a center-of-mass energy of $\sqrt{s_{NN}} = 5.02\,\text{TeV}$ [11]. A TOF[5] for velocity determination is installed between

[4]Inner tracking system
[5]Time of flight

the TRD[6] and the EMCal[7]. All sub-detectors are enclosed in a solenoid, which creates a magnetic field of 0.5 T for trajectory bending and therefore momentum determination. Figure 1.4 gives a schematic overview of the ALICE detector. One of the key features of ALICE is its excellent PID capability [8]. Particles are identified by reconstructing their momentum, energy and charge. Their velocity is determined by either the measurement of the specific energy loss $\mathrm{d}E/\mathrm{d}x$, as for example in the TPC, or their traversing time between the collision point and detection in the TOF [9].

ALICE will be upgraded to further investigate effects like heavy-quark production at low transverse momenta, interaction in the QGP, quarkonium production, the partonic equation of state and exotic hadronic states [12].

Currently, signal amplification in the ALICE TPC is achieved with MWPCs. During the time when the gating grid is closed, incoming charges are blocked at the gating grid, which effectively renders the detector blind. The electron drift time of $\sim 100\,\mu\mathrm{s}$, as well as the $\sim 180\,\mu\mathrm{s}$ lasting gated neutralization process impose rate limitations of $\sim 3.5\,\mathrm{kHz}$ for the readout [2]. The LHC will raise its interaction rate in RUN 3 to 50 kHz. Therefore, the gated MWPC readout is insufficient, as it would impose an unacceptable loss of events. In order to be prepared for the luminosity upgrade, the MWPC-based readout will be upgraded with a GEM-based one.

1.4 Gas Electron Multiplier

A typical GEM [13] consists of a thin polyimide foil (thickness $\sim 50\,\mu\mathrm{m}$) with copper ($\sim 5\,\mu\mathrm{m}$) layers applied on both sides. It is perforated with holes in a hexagonal arrangement. An electron microscope image of a GEM is depicted in Fig. 1.5. The holes are etched in a photo lithographic process from both sides, resulting in a double-conical shape with an inner radius of $\sim 50\,\mu\mathrm{m}$ and an outer radius of $\sim 70\,\mu\mathrm{m}$. The distances between the holes are typically $\sim 140\,\mu\mathrm{m}$, but also pitches of $\sim 90\,\mu\mathrm{m}$ and $280\,\mu\mathrm{m}$ are possible. Voltages are applied to the upper and lower GEM electrode, resulting in a potential difference of several hundred volts. In the center of the holes high field strengths of typically $\sim 50\,\mathrm{kV\,cm^{-1}}$ emerge [14], which are sufficiently high for avalanche multiplication. Single GEMs can deliver gains of up to $\mathcal{O}(10^3)$, while higher gain and enhanced operational stability can be achieved by sharing the gain between several GEMs, which are subsequently stacked [16]. Figure 1.6 shows a cross-section of a GEM and the result of a simulation of the amplification process. Two electrons enter the amplifying region from the drift region. The red lines indicate

[6] Transition Radiation Detector
[7] Electromagnetic Calorimeter
[8] Particle identification
[9] Time of Flight

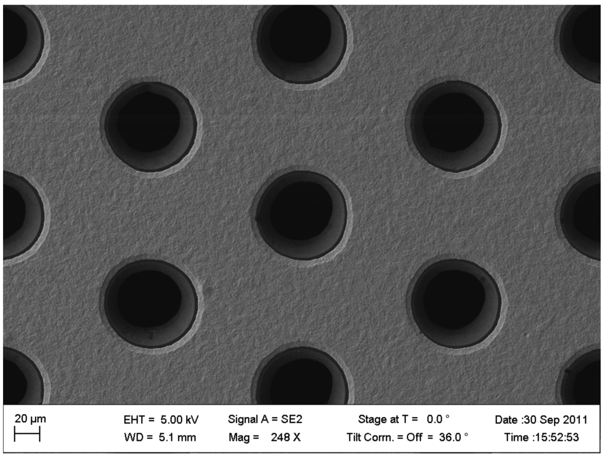

Figure 1.5: Top view of a GEM foil photographed by a electron microscope. (Pitch 140 µm) [2].

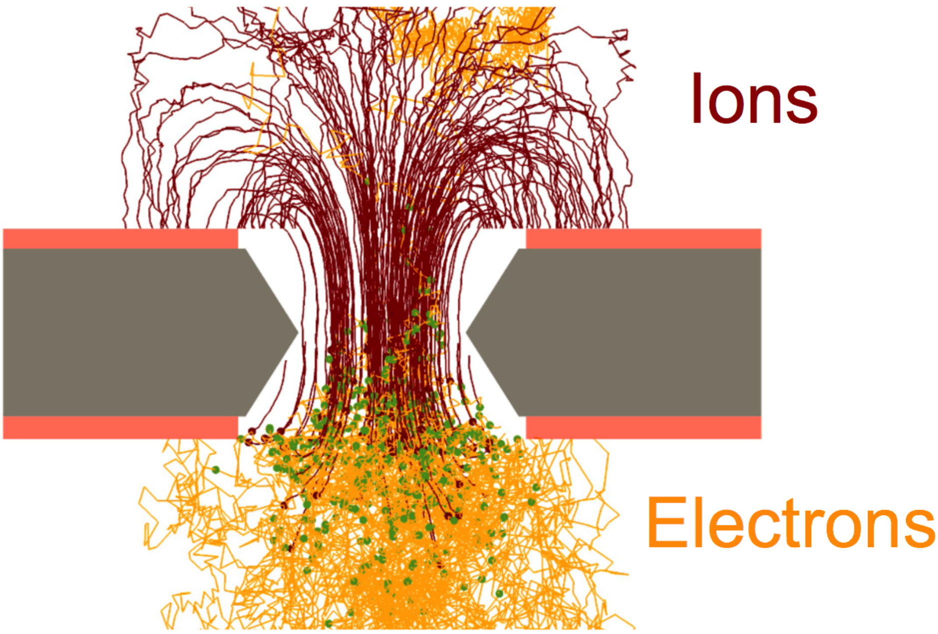

Figure 1.6: Garfield/Magboltz simulation of two electrons entering the GEM-amplification region. Ion paths are in red, electron paths in yellow. Green dots represent points of ionization [15].

the ions' tracks, which are produced in the amplification process. Notably, almost all ions are collected on the upper side of the GEM, while most electrons are extracted. This so-called intrinsic ion backflow suppression blocks ions from backdrifting into the active volume.

1.4.1 Raether Limit

Crucial for the stable operation of a GEM-based detector is the prevention of electric discharges. When the electron density in the amplifying region grows to high values, discharges are believed to occur. The so-called Raether Limit [17] is the critical value of created electrons in the amplification process before a discharge occurs in parallel-plate detector and is given as following

$$Q_{\mathrm{crit}} = G_{\mathrm{max}} \cdot N_{\mathrm{primary}} \sim 10^8 \mathrm{electrons} \tag{1.1}$$

with G_{max} being the maximum achievable gas gain and N_{primary} the amount of primary created electrons [18]. The situation in GEMs are expected to be similar, as GEM holes can only cope with a certain number of electrons before a discharge occurs.

1.4.2 Discharges

GEMs operate in the harsh environment of high-rate experiments and several aspects like heavily ionizing particles, micro particles or residual dust and sharp edges, from which enhanced electric fields emerge, can contribute to an increased discharge rate. When a discharge occurs, a conductive link between upper and lower GEM electrode emerges, leading to an alignment of the potentials. Until the potentials are fully retained, the amplification process is interrupted. The recharging of the GEM by the power supply can take several milliseconds in which the detector is effectively rendered blind. The energy released by a discharge may also be threatening to the readout. The streamer model is believed to explain the creation of sparks triggered from a single electron avalanche. Figure 1.7 shows a schematic of a streamer in a parallel-plate detector. Occasional transitions from the nominal amplification to the streamer mode may occur at high electric field strengths. Charge separation occurs, as the electrons drift to the cathode and ions to the anode. The creation of a streamer is characterized by an exceeding of the Raether limit. The emerging high electric fields in the streamer are directed anti-parallel to the electric field of the parallel plate detector, but comparably strong and trigger a self-induced avalanche multiplication, which enlarges the streamer. Most of the time, the streamer then forms a conductive link between the cathode and the anode and a discharge is induced [18].

Furthermore, secondary discharges, which follow after an initial discharge, have been observed [20]. Even though many hypotheses try to explain this phenomenon,

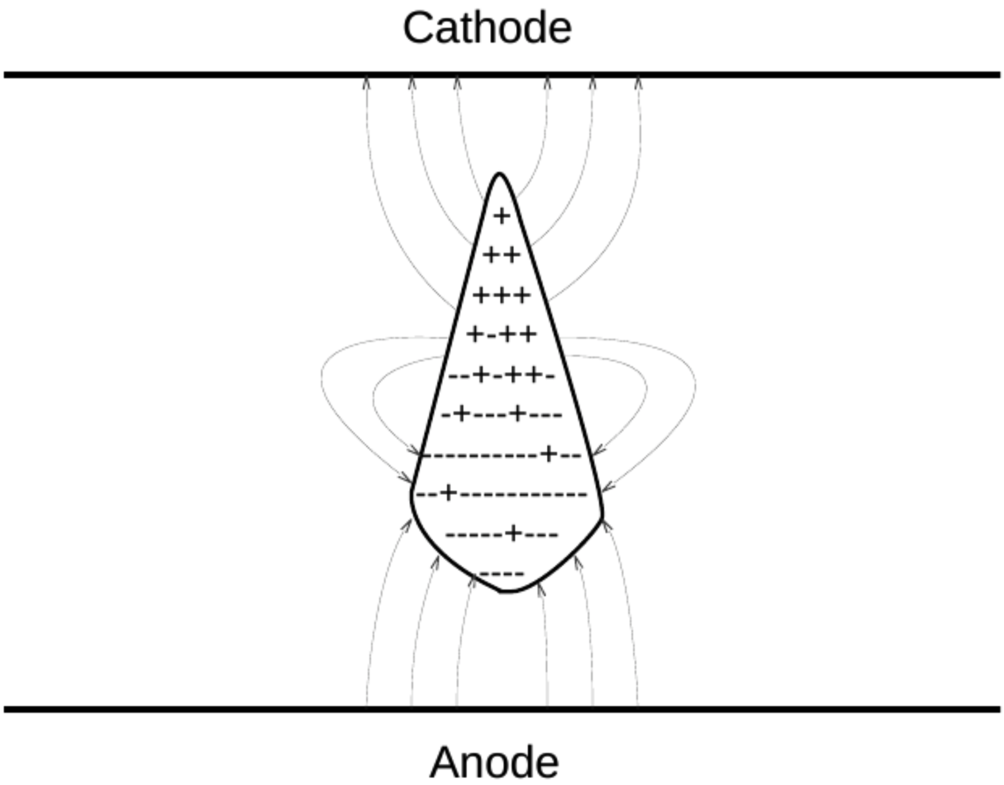

Figure 1.7: Schematic of a streamer-droplet in a parallel-plate detector [19].

it is not fully understood yet. Secondary discharges are characterized by larger amplitudes than the amplitude of initial ones. Secondary discharges may be related to the propagation between adjacent GEMs in the stack or between GEM and readout and may be harmful as much energy is released.
Streamers are a possible explanation for the occurrence of secondary discharges and can be initiated in several ways. High-energetic photons released by the initial discharges create dense clouds of electrons and ions, in which a streamer can form. As photons spread with the speed of light, this process follows almost instantaneously to a discharge. Another possible explanation is, that after a discharge the work function of the electrode is lowered, due to the bombardment of the GEM surface by the ions freed in the course of the spark. Combined with the constantly created charge by traversing alpha particles in the vicinity of the discharge region, a streamer can emerge in the high external electric fields.
The discharge probability is defined as following

$$P = \frac{N}{tR} \tag{1.2}$$

with the number of discharges N within the measurement time t and R being the rate of the source. The statistical error of the discharge probability is then given by the following equation

$$\Delta P = \frac{N}{tR}\sqrt{\left(\frac{\sqrt{N}}{N}\right)^2 + \left(\frac{\Delta R}{R}\right)^2} \tag{1.3}$$

with ΔR being the statistical uncertainty of the source rate [21]. The number of discharges N is assumed to be poisson distributed, therefore, the uncertainty of N is

$$\Delta N = \sqrt{N} \tag{1.4}$$

ΔR is then defined to:

$$\Delta R = \frac{\sqrt{N}}{t} \tag{1.5}$$

Chapter 2

Software development

In order to observe the phenomenon of secondary discharges, large amounts of pulse shapes were analyzed. Therefore, automated data acquisition was necessary to observe the signals of initial and secondary discharges. As the measurement devices communicate with PCs via LabVIEW, the corresponding software was developed in the course of this thesis to detect and store pulse shapes from an oscilloscope as well as to automate gain measurements with the Keithley electrometer.

2.1 Labview

LabVIEW [22] is a development environment, which was developed by National Instruments in 1986. Its key features are data acquisition, the control of measurement instruments and automation of processes. It is a so-called visual programming language. The software code is created by connecting several VIs[1] via wires. VIs are functions combined in blocks of code. Data is being transported on block diagrams by connections called wires. LabVIEW also automatically generates an user interface to manage the users in and output. National Instruments provides a large database of drivers to connect measurement devices with LabVIEW. LabVIEW comes with a companion software called NI MAX[2], which manages the data transfer between the device and the PC.

2.2 Keithley electrometer

The Keithley 6517b [23] ampere meter is a fast high precision measurement device for very low currents in the magnitude of 10^{-15} A. This device is also able to measure resistance, charge and voltage. It is compatible with LabVIEW and communicates via GPIB[3]. The device is connected via USB to a Windows PC.
Primary ionization in the drift volume only creates very low currents, which need

[1] Virtual Instruments
[2] Measurement & Automation Explorer
[3] General Purpose Interface Bus

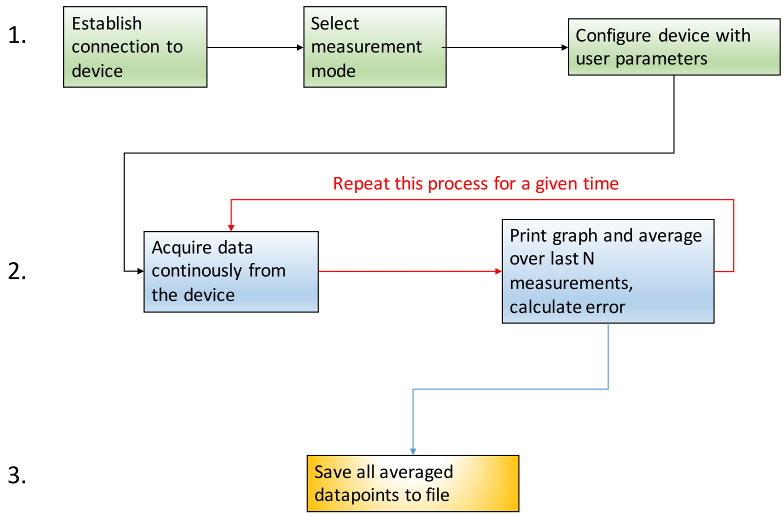

Figure 2.1: Basic principle of the Keithley LabVIEW software

to be amplified via a GEM structure by a factor of $\mathcal{O}(10^2 - 10^3)$. However, the secondary currents are still very low ($\mathcal{O}(10^{-9}\mathrm{A})$). Additionally, the signal is fluctuating strongly due to background noise, whose contribution can be reduced by taking many measurement values and averaging them. The LabVIEW software, which was developed in the course of this thesis, automatizes the measurement process and stores the acquired data and parameters on the PC. The schematic principle of the software is displayed in Fig. 2.1:

1. First, there are several pre-operational steps. After connecting the device, the software is initializing the connection. Following that, the device is set to the desired measurement mode (voltage, current, charge or resistance). Now the Keithley is configured with user-given parameters, like measurement range and time, number of values to average and integration time on the frontpanel shown in Fig. 2.2.

2. When the parameters are configured, the device is continuously acquiring measurements for a specified time. During this process, the measurements are monitored and the average of the last N measurements as well as its standard deviation is displayed.

3. When the measurement time ends, all averaged data points, as well as the corresponding standard deviations are saved to a text file.

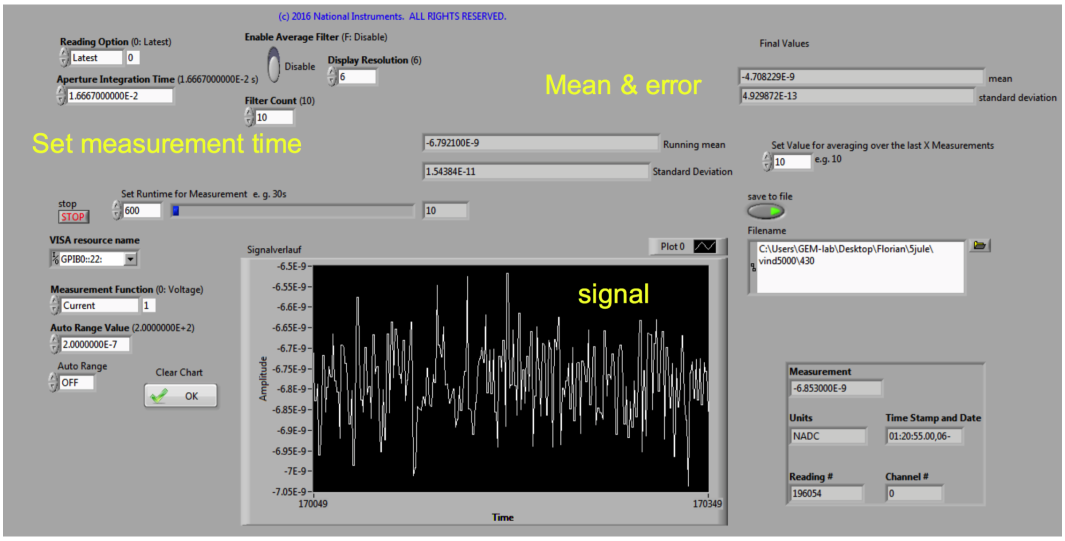

Figure 2.2: The Keithley frontpanel. User input is highlighted in white, output in grey. The last measurement values are displayed on the black graph.

2.3 Tektronix oscilloscope

Discharges manifest in short signals with high amplitudes. A pulse shape analysis of the secondary discharges should provide a further understanding of their origin. In order to track and analyse their pulse shapes, an oscilloscope with high precision and time resolution, as well as the ability to store the pulses, is necessary. Therefore, in the scope of this thesis, LabVIEW software to configure the Tektronix MSO PDO 4104b oscilloscope [24] and store pulse shapes was developed. The oscilloscope from Tektronix has a bandwidth of up to 1 GHz for fast signal processing as well as a sampling rate of 5 GS/s. It is able to capture 340000 waveforms per second and can acquire up to 20 million points per pulse shape. The DPO 4104b is able to trigger on fast changes in the signal in many different options. The conditions to recognize a discharge is an exceeding of a threshold value by the signals amplitude as well as a either falling or rising slope. The acquiring process of this software is schematically drawn in Fig. 2.3.

1. The software establishes a connection to the device. Afterwards, the device is configured by user-given parameters, such as measurement range, trigger mode, number of points per waveform, time intervals and the saving directory.

2. In acquisition mode, the oscilloscope is set to triggering status, waiting for a signal to fulfill the triggering requirements.

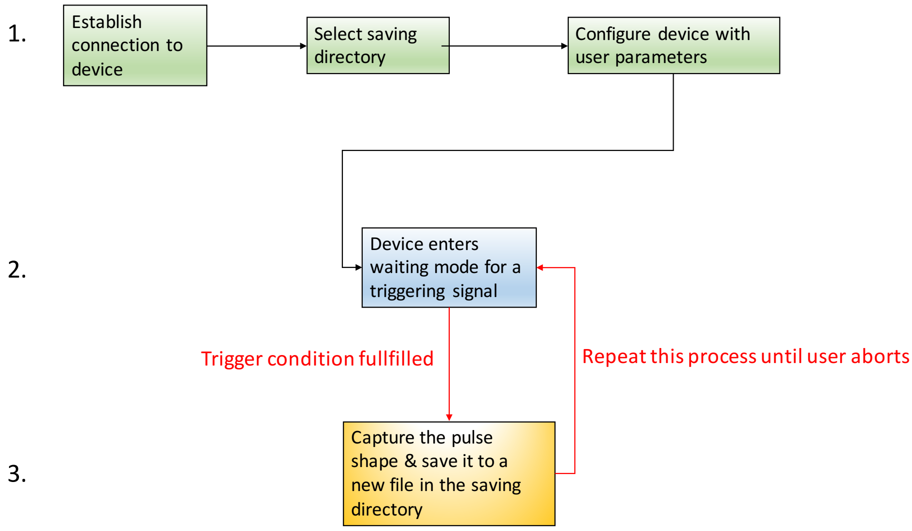

Figure 2.3: Basic principle of the Tektronix oscilloscope LabVIEW software

3. If this happens, the device saves that waveform, samples and displays it on the screen and proceeds that information to the PC. At that moment, a time stamp is also generated to obtain information about the exact time of the trigger. Finally the captured waveforms are saved to disk.

The oscilloscope has a hardware-related dead time of around 300 ms after every captured event. To prevent multi-triggering due to a multiple fulfillment of the trigger conditions by signal oscillations, the oscilloscope is reconfigured after every triggered event, which further reduces the readout rate. The oscilloscope is able to distinguish between 340.000 waveforms per second, while the actual saving rate is much lower. In order to determine the saving rate of the device, periodical pulses are created and then saved. Figure 2.5 shows the efficiency $\frac{N_{\text{saved}}}{N}$ for various signal pulse rates. N_{saved} is the amount of completely saved pulses by the oscilloscope setup, while N is the amount of created pulses. The setup's maximal capture rate at an efficiency of 100% can be determined to 0.35 Hz, which is sufficient for the study conducted in the scope of this thesis. The efficiency quickly drops to much lower values at higher frequencies.

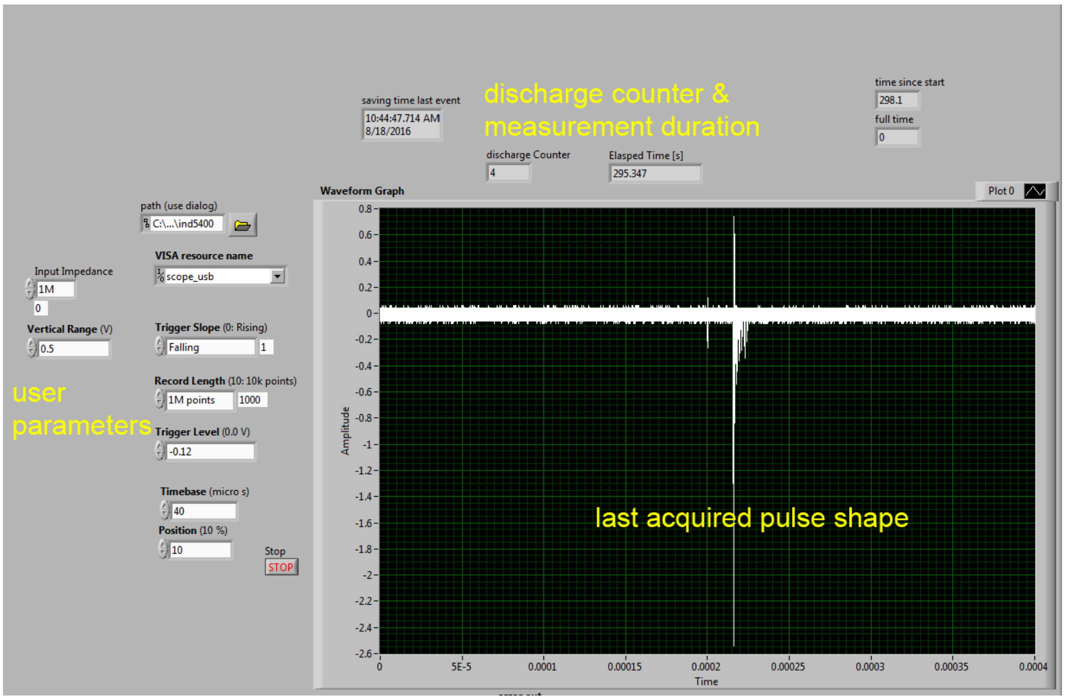

Figure 2.4: Frontpanel of the oscilloscope LabVIEW software. User parameters can be configured on the left side. The graph always shows the last sent pulse shape from the oscilloscope.

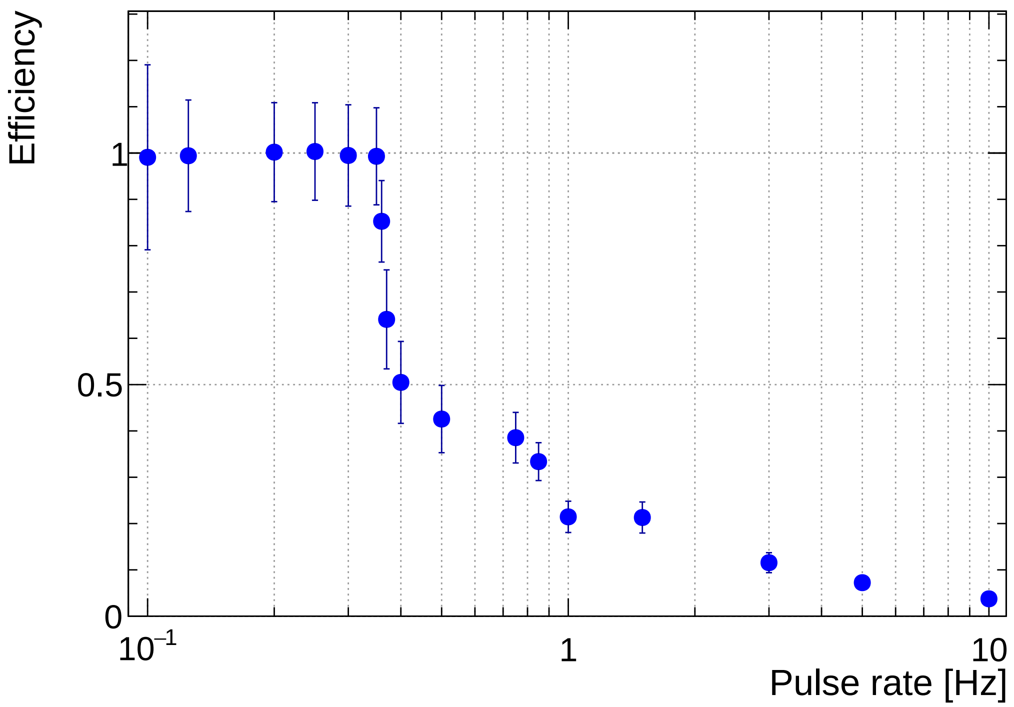

Figure 2.5: Oscilloscope saving efficiency as a function of the pulse rate.

Chapter 3

Detector Setup

In order to investigate the phenomenon of discharges, a detector setup has been commissioned in different HV configurations with various readout approaches and sources in Ar-CO_2.

3.1 Detector and readout system

The detector consists of a metallic box with removable lid. Figure 3.1 is a photo of the arrangement of cathode, GEM and cathode with the source on top. The detector contains a quadratic 10 cm x 10 cm segmented pad plane with inner and outer section. The GEM-foil is placed above the anode at a distance of 2 mm or 3 mm, which defines the induction gap. Pillars are installed on all corners and hold the cathode plane at a height of 2 cm with respect to the anode. The radioactive source is placed on the cathode and is emitting radiation through a hole with 8 mm diameter into the

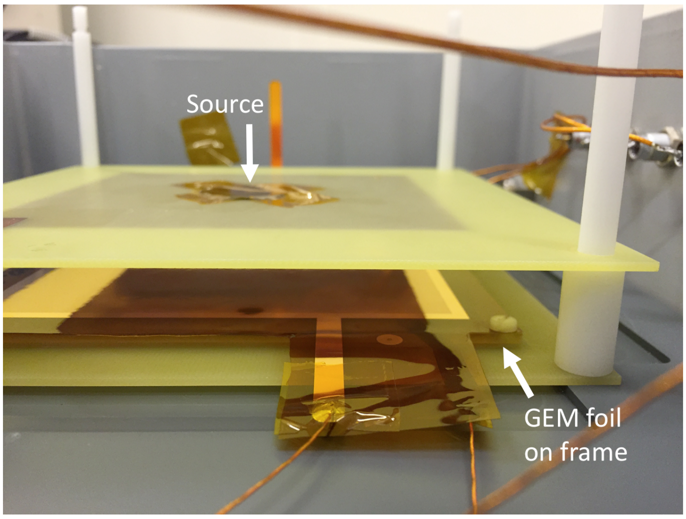

Figure 3.1: Picture of the detector taken from the side. Source and foil are indicated.

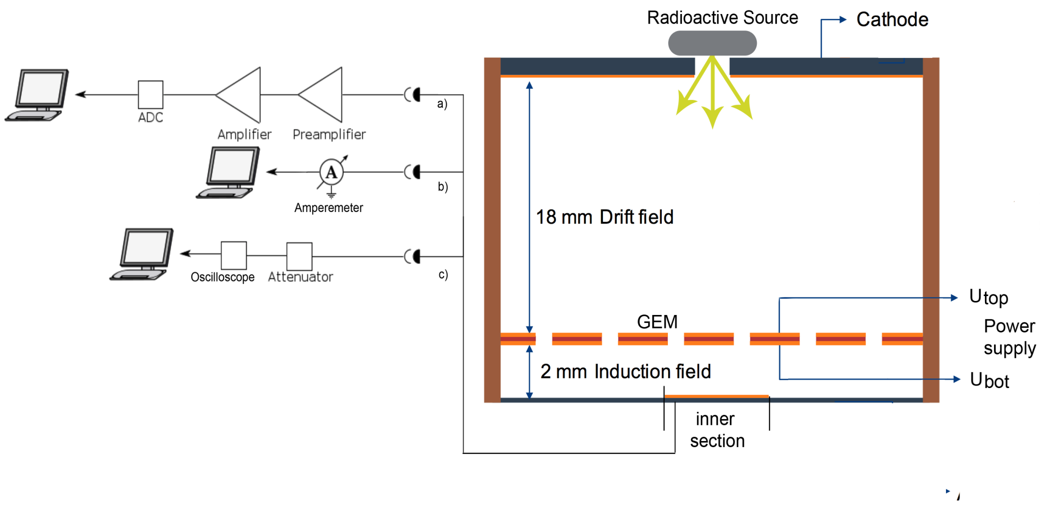

Figure 3.2: Schematic of the detector for a single GEM setup with 2 mm induction gap. The source is placed on top of the cathode with the active side pointing downwards. a) Readout path for the spectrum measurement, b) Readout path for gain measurements, c) Readout path for the capturing of discharge pulse shapes.

drift volume and thus allows for the irradiation of the active detector volume. The corresponding drift length is 18 mm for a 2 mm induction gap and 17 mm for a 3 mm induction gap, respectively. Because there is no field cage installed at the edges of the active volume, the drift field is only uniform in the center and is expected to be distorted towards the outer regions. Therefore, only the inner section, which is an area of 8 cm x 8 cm is read out. The outer area is grounded with 50 Ω to match the impedance of the inner section, which arises from the termination of the electronics. Figure 3.2 shows a schematic of the detector and the three readout variants, as discussed in Sec. 3.1.3. The detector is flushed with a gas mixture of Argon and CO_2 as discussed in Subsec. 3.2 and it is ensured that the amount of O_2 molecules in the volume is kept sufficiently low in the order of 10^{-6}. Oxygen significantly reduces the gain due to its high electronegativity.

3.1.1 GEM foils

All measurements have been carried out with 10 cm x 10 cm GEM-foils in standard hole pitch configuration as discussed in Sec. 1.4. To assure a high quality of the GEM foils, several preparational steps are mandatory. The foils are produced at CERN and then shipped to TUM, where they are inspected in a HV test. A potential difference of 550 V is applied between upper and lower side. In a time interval of around 10 min, the number of discharges is monitored, as well as the leakage current. The latter should not exceed several nA. Otherwise, there is an ohmic connection between the GEM electrodes which prohibits usage of that specific foil. Responsible for such connections are often dust or other small particles on the foil's surface. Following this first test, the foils are thermally stretched in an oven. Afterwards, foils are carefully glued centrally on a frame with the epoxy ARALDITE 2011 [25] followed by a curing session of at least 24 h at 60 °C. In a last step, the stretching tools are removed, unnecessary parts are cut off and a final high voltage test is performed to ensure stability.

3.1.2 HV setup

The measurements have been conducted in the HV setup as depicted in Fig. 3.3. Both GEM electrodes are powered by independent power supply channels. The potentials on the cathode and the GEM electrodes are adjusted via a EHS F 060n ILK power supply from iseg [26]. A resistor to ground with 10 MΩ is connected in series to the lower GEM side as well as a 5 MΩ resistor to ground being connected to the upper GEM electrode, which result in a constant current. In case of a HV trip, the current limit of the power supply is exceeded and it shuts down. This assures a safe discharge of the GEM foils. Additional loading resistors R_{top} and R_{bot} are connected in series to the corresponding GEM electrodes and varied to study their impact on the discharge behavior of the system and to decouple the GEM from the parasitic capacity of the HV system. Table 3.1 depicts the various standard and flipped resistor configurations.

Table 3.1: Resistor configurations for standard and flipped.

	$\mathbf{R}_{\text{top}}$ [Ω]	$\mathbf{R}_{\text{bot}}$ [Ω]
Standard	10 M	0
Flipped	0	10 M
Standard + 10 kΩ	10 M	10 k
Flipped + 10 kΩ	10 k	10 M

3.1.3 Readout

The detector is read out in three different approaches, as depicted in Fig 3.2.

a) The detector's energy resolution is determined with a MCA[1] [27]. Signals coming from the detector's anode are preamplified and shaped. The spectral

[1] Multi channel analyzer

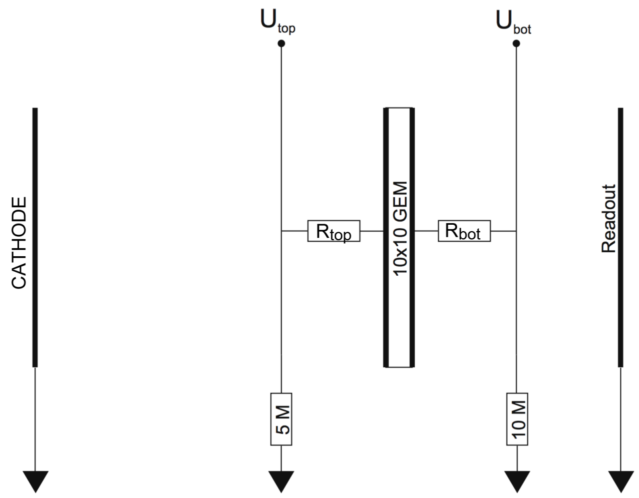

Figure 3.3: Schematic of the HV setup, modified from [20].

analyzer then counts those shaped signals and also determines the amplitude of the signal, which is directly proportional to the energy deposited in the active volume.

b) In order to determined the gain, the detector's readout anode is directly connected to the Keithley amperemeter, which measures the current.

c) To store discharges, the detector's readout anode is connected to an attenuator to lower the signal's amplitude. Discharges are high energetic signals and a direct connection to the oscilloscope would exceed the measurement range and pose a threat to the device itself, due to the large amount of charge. Thus, they are attenuated with 34 dB.

Afterwards, the data is processed with ROOT.

3.2 Gas

The detector is flushed with a gas mixture of 90% Argon, with a purity larger than 99.999% and 10% CO_2, which is added as a quencher. Photons with an energy, which is too low to ionize the detector gas are also created in the amplification process. They can create free charges on metallic surfaces in the detector via the photoelectric effect. As these charges aren't induced by the primary ionization process, they impair the measurement process of trajectories. Quencher are molecular gases with rotational and vibrational states and are added to absorb these low-energetic photons. Argon is a noble gas and its filled atomic subshells make it chemically stable with a high ionization energy. Charged particles, which move through the argon gas, deposit energy in inelastic collisions with the gas atoms and molecules and ionization occurs. The effective ionization potential W_i is the amount of energy, which needs to be transferred, to create one ion-electron pair. For gas mixtures, it is determined by the following formula

$$W_{i,n} = \frac{\sum\limits_i x_i \cdot W_i}{\sum\limits_i x_i} \tag{3.1}$$

with x_i being the fraction of gas i and W_i being the related ionization potential [2]. The effective ionization potential for Argon-CO_2 in 90-10 is 28.19 eV. In the course of this thesis only Ar-CO_2 (90-10) was used.

3.3 Radioactive sources

Radioactive sources emit particles in the decay process. α sources emit positively charged ${}^4_2$He nuclei, which can traverse several centimeters in air before being neutralized. β radiation consists of free moving electrons, which can travel several meters. When α or β particles are travelling through gas, they deposit a fraction of their energy in inleastic collisions with the shell electrons of the gas atoms. The energy deposit per unit path length dE/dx in matter is given by the Bethe-Bloch formula [28]. Pairs of electrons and ions are created along the trajectory of the initial particles. γ sources emit photons, which ionize gas atoms mainly by photoabsorption.
For gain determination, a ^{55}Fe source was employed. ^{55}Fe decays by electron capture with a half-life of 2.737 years to the stable ^{55}Mn isotope. The emitted γ yields an auger-electron with a probability of 60 % and an energy of 5.19 keV, which gets mainly absorbed in the material of the source. ^{55}Fe also emits photons from K_α transitions with energies of $\sim$ 5.9 keV [29]. Electrons are emitted via the photoelectric absorption of the photons by the gas atoms and ionize the detector gas. In argon, a second peak, the so-called single escape peak appears in the spectrum. The energy $E_{\gamma,\text{escape}}$ of the single escape peak in argon is 2.89 keV and it is created from photoabsorption in the K-shell. When the atom de-excites, an electron from an outer shell (e.g. L-shell) is filling the free spot in the K-shell and a photon is emitted, with an energy corresponding to the energy difference between the K and L shell. This energy is too low for further gas ionization and the photon leaves the detector volume. Therefore, not the full energy is deposited in the active volume.

For discharge measurements, a mixed source, consisting of the α-sources ^{239}Pu, ^{241}Am and ^{244}Cm was employed. The corresponding weighted energies of the emit-

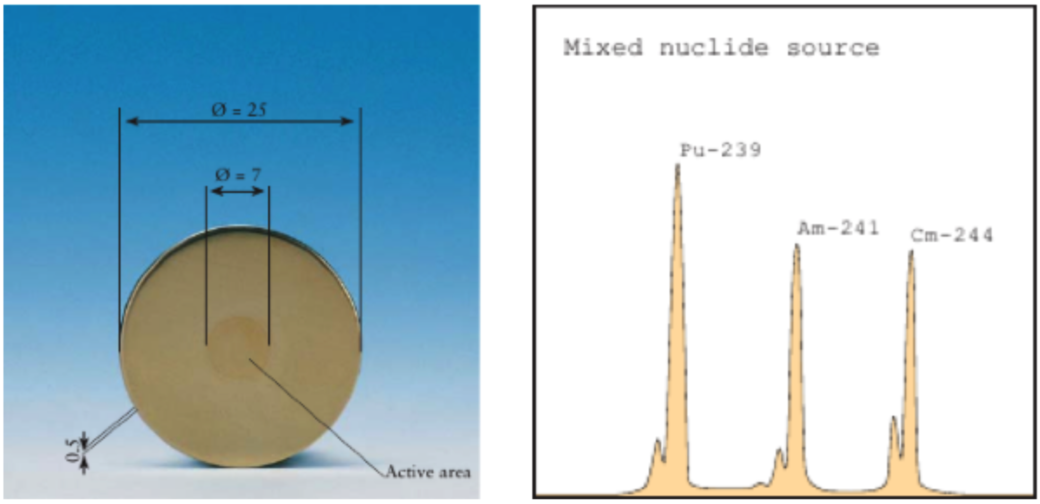

Figure 3.4: Picture of the mixed source with the corresponding spectrum [30].

ted ${}^{4}_{2}$He nuclei are 5.155 MeV, 5.486 MeV and 5.805 MeV [30]. The source has an activity of 3 kBq. The spectrum is depicted in Fig. 3.4.

Chapter 4

Detector commissioning

4.1 Energy resolution

The detector's energy resolution is determined by measuring the energy spectrum of a reference source, like ^{55}Fe, in Ar-CO_2 with a MCA spectral analyzer, as depicted in Sec. 3.1.3. The spectrum was recorded at a $\Delta U_{\text{GEM}} = 460\,\text{V}$ and an induction field strength of $3\,\text{kV}\,\text{cm}^{-1}$. Clearly visible is the 5.9 keV absorption peak in red and the escape peak with 3.0 keV in blue. The exponential background signal is indicated in green. The fit is the sum of the two Gaussian fits and the exponential fit for the background. The energy resolution ΔE is determined by

$$\Delta E = \frac{\sigma}{\mu} \tag{4.1}$$

for each peak, with μ being the mean and the standard deviation being σ. Afterwards, the fit results of the two Gaussian are weighted with their amplitude and normalized. The energy resolution can be determined to (8.83 $\pm$0.04)%. The uncertainty calculation of the resolution is depicted in Sec. A. The uncertainty values stem from the errors of the fit parameters. The energy resolution is highly dependent on the oxygen content in the detector volume. Oxygen is very a very electronegative element and reduces the primary ionization significantly. Additionally, the energy resolution is altered by gain fluctuations. As a result, the Gaussian peaks in the spectrum are broadened.

4.1.1 Rate of the ^{55}Fe Source

The rate is determined by measuring the spectrum at a high gain and then fitting the spectrum, as discussed in Sec. 4.1. Afterwards, the integrated area of escape and absorption peak is divided by the measurement duration. The rate of the ^{55}Fe source in the detector has been determined to (625 $\pm$ 3) Hz. The uncertainty is calculated by taking into account the errors of the fit parameters.

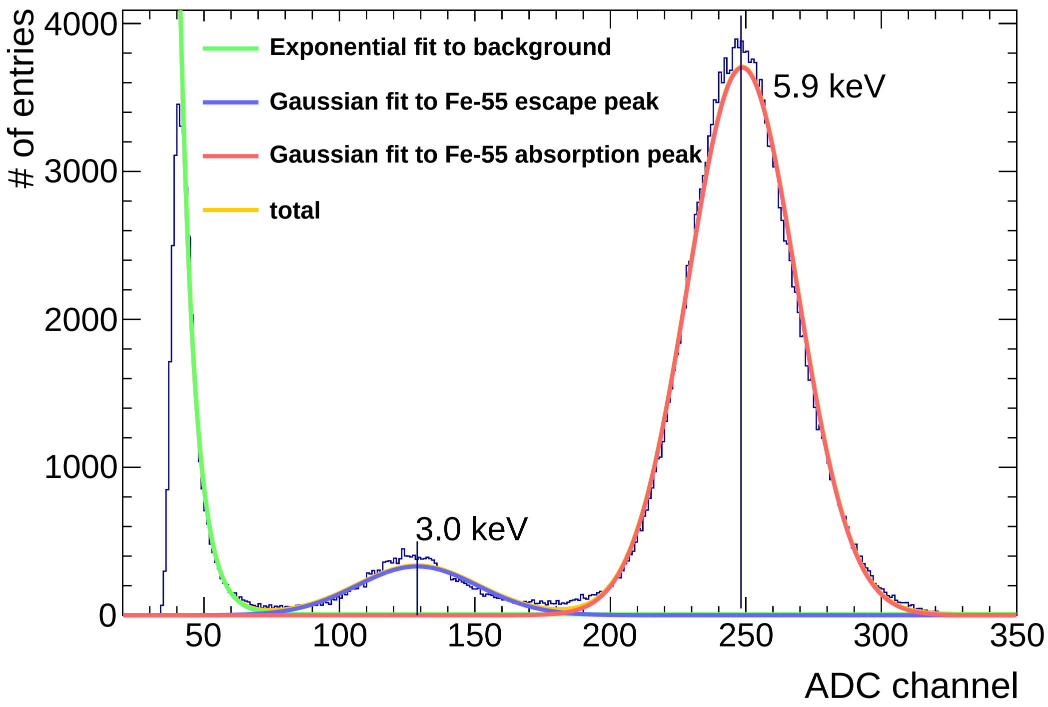

Figure 4.1: Energy spectrum of the ^{55}Fe source. Indicated are the fitted functions.

4.1.2 Rate of the mixed source

Figure 4.2 shows the energy spectrum of the mixed source, measured with the detector at a ΔU of 340 V and an induction field of $E_{\text{ind}} = 3\,\text{kV}\,\text{cm}^{-1}$. The background on the left side is clearly separated from the source's signal. Due to the limited spatial acceptance and the detector's energy resolution, the spectrum exhibits a broad distribution. The visible rate in the detector is calculated to (479.3 ± 0.6) Hz by integrating the bins between the ADC channels 4000 and 10000 and dividing the sum by the measurement duration. The uncertainty is determined by varying the lower bounds of the integral between 2000 and 4000. The sharp edge on the right side comes from the fact, that the spectrum analyzer is in saturation due to high energy signals.

4.2 Gain measurements

The primary current is defined as the current in the active volume due to the ionization of the gas by incident particles. When passing through the GEM, the primary current is amplified and extracted on the lower GEM-side, which is the so-called

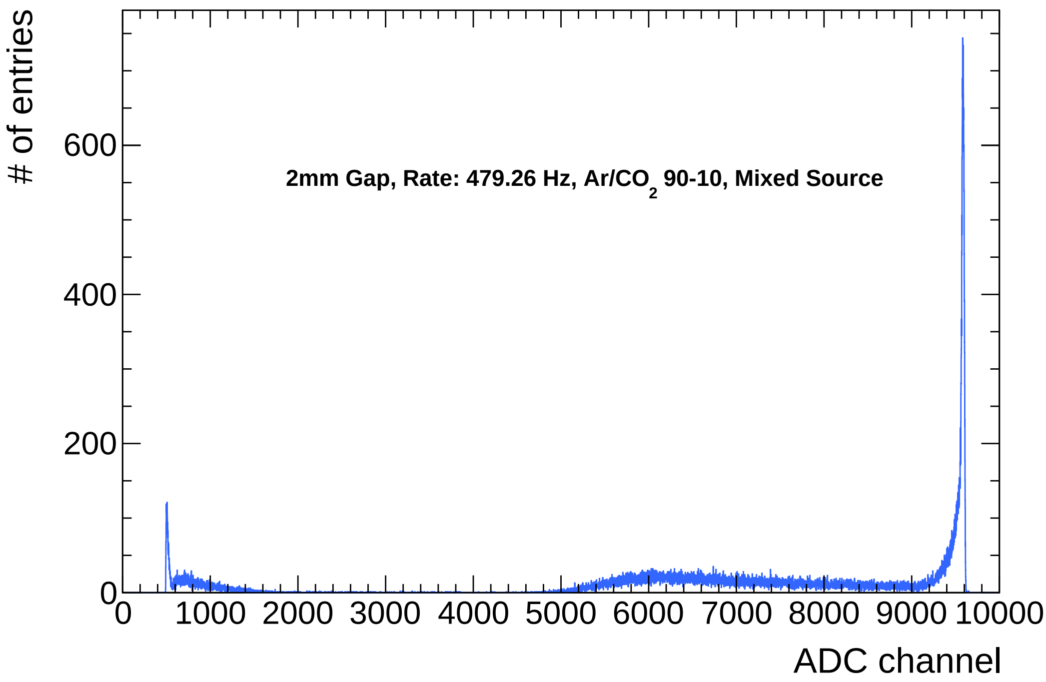

Figure 4.2: Energy spectrum of the mixed source.

secondary current. The effective gain is determined as the ratio of the secondary and the primary current,

$$G = \frac{I_{\text{secondary}}}{I_{\text{primary}}} \tag{4.2}$$

The secondary current is directly measured on the anode with the Keithley 6517b, as depicted in Fig. 3.2 b).

I_{primary} of α sources is determined by applying a drift field and measuring the current on the upper GEM electrode with the Keithley similar to path b), while the lower GEM electrode and the readout are grounded. For ^{55}Fe, the primary current is calculated from

$$I_{\text{primary}} = n \cdot e \cdot R \tag{4.3}$$

with the rate R of the source in the detector. The rate is measured with the MCA as already discussed in Sec. 4.1. The number of electrons n is determined by:

$$n = \frac{E_{\text{radiation}}}{W_I} \tag{4.4}$$

$E_{\text{radiation}}$ is the energy of the emitted radiation by the source and W_{I} is the effective ionization potential.

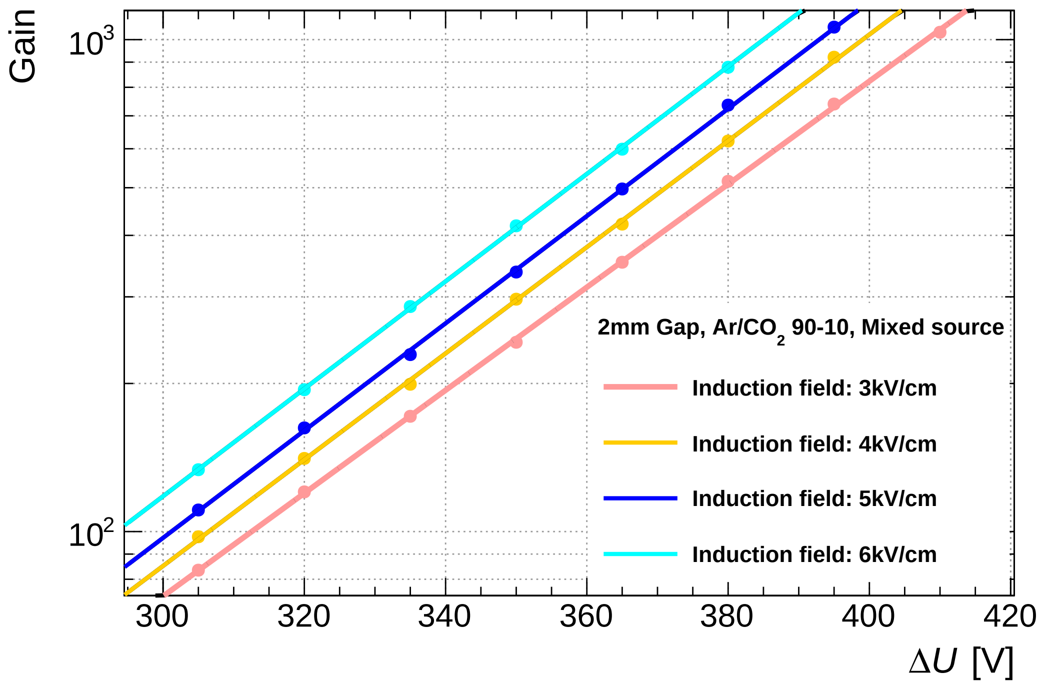

Figure 4.3: Gain as a function of ΔU over the GEM for various induction fields.

The gain has been determined for various induction fields. Figure 4.3 depicts the gain as a function of the potential difference applied to the GEM for several induction field strengths. Additionally, the exponential fits are indicated. There is a slight dependence of the gain on the field strength due to enhanced charge extraction from the bottom side of the GEM electrode at higher fields. This can also be observed in Fig. 4.4, which shows the gain at a constant $\Delta U = 407\,\mathrm{V}$ applied to the GEM for various induction fields. Indicated are several measurement points and the exponential fit.

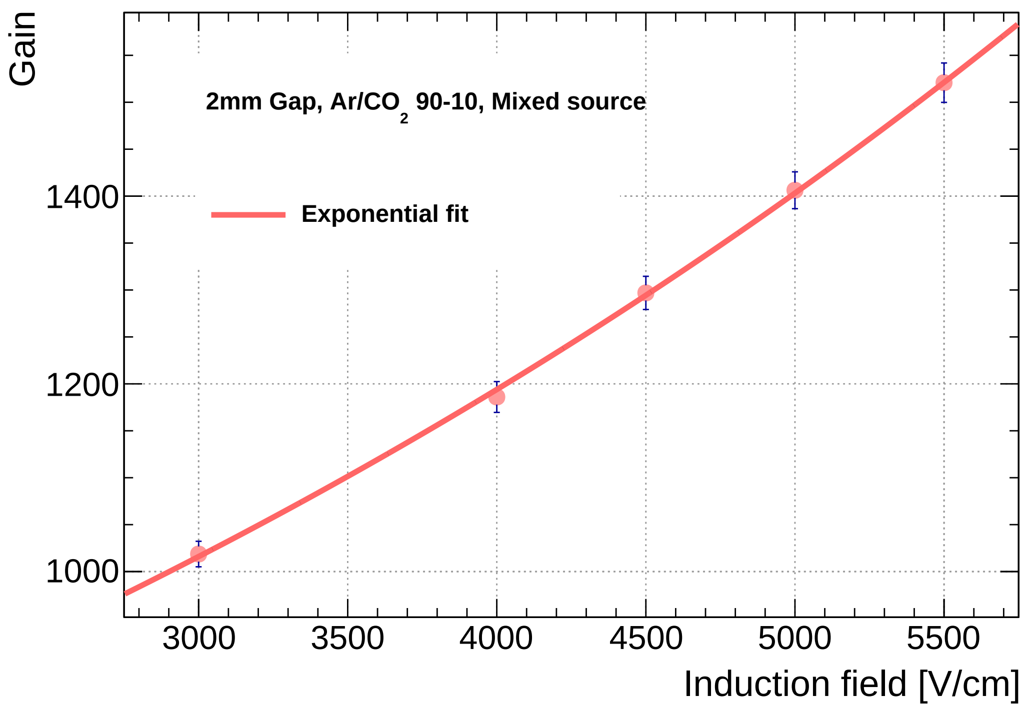

Figure 4.4: Effective gain as a function of the induction field by a constant $\Delta U = 407\,\mathrm{V}$ over the GEM.

Chapter 5

Discharge studies

This chapter presents the results of the discharge studies. The phenomenon of secondary discharges has been observed in several circuit configurations to determine the dependency of loading resistors. Moreover, the dependency of the probability for secondary discharges on the values of the loading resistors has been studied. All measurements have been done at a ΔU of 407 V.

5.1 Initial discharges

The shape of an initial discharges resembles that of an oscillating signal, whose amplitude reduces exponentially, as depicted in Fig. 5.1.

5.1.1 Discharge probability

The discharge probability has been observed as a function of the induction field. Figure 5.2 shows the discharge probability for various HV configurations, as discussed in Sec. 3.1.2. The discharge probability slightly increases with the applied induction field strength, but stays in the order of $\sim 10^{-5}$. Considering the rate of the source in the detector, the discharge rate is low enough to capture all discharges with the setup. The probability is independent on the configuration of the powering scheme as discussed in 3.1.

5.1.2 Study of the signal oscillations

The oscillations of the signal were investigated by comparing the times values of the local extrema of the initial discharges. The noise of the signal was smeared out by averaging the signal in five measurement point steps. Afterwards, local maxima and minima were identified by sampling the signal in intervals of five points. This method has proven to reliably yield the extrema. The time differences between the spikes of the oscillations were collected in a histogram and fitted with a Gaussian. Figure 5.3 depicts the time values between the oscillation spikes, which are independent of the applied induction field within the uncertainties. For a length of the coax cable

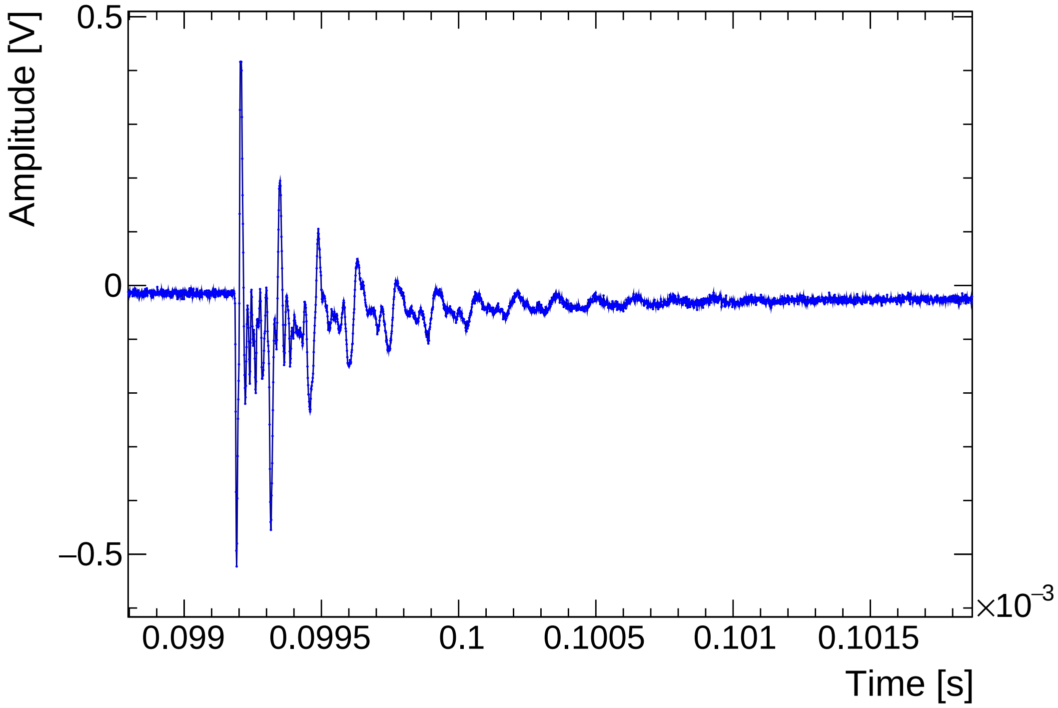

Figure 5.1: Pulse shape of an initial discharge.

of 1.05 m the period has been measured as (57 ± 10) ns.

The power supply is connected via coaxial cables to the GEM electrodes with an estimated capacity of $\sim 100\,\mathrm{pF\,m^{-1}}$. The inductivity of a coaxial cable is given by the expression

$$L = \frac{\mu_0 \mu_r l}{2\pi} \cdot \ln\left(\frac{R}{r}\right) \tag{5.1}$$

where μ_r is the permeability of the dielectric, μ_0 is the vacuum permeability, R is the radius of the outer copper shield, l is the cables length and r is the radius of the inner copper core. The dielectric inside of the coaxial cables is polyethylene, which has roughly a μ_r of 1. Inner and outer diameter in the cable are 3.7 and 6.15 mm. The inductivity is then determined to $\sim 11\,\mathrm{\mu H}$.

GEM and coaxial cables can be approximated by a LC circuit, whose resonance frequency is given by

$$f_0 = \frac{1}{T} = \frac{1}{2\pi\sqrt{LC_{\mathrm{comb}}}} \tag{5.2}$$

with L being the circuit's inductivity and C_{comb} being the capacity. C_{comb} is determined as the spare capacity of a series connection of the GEM capacity and the

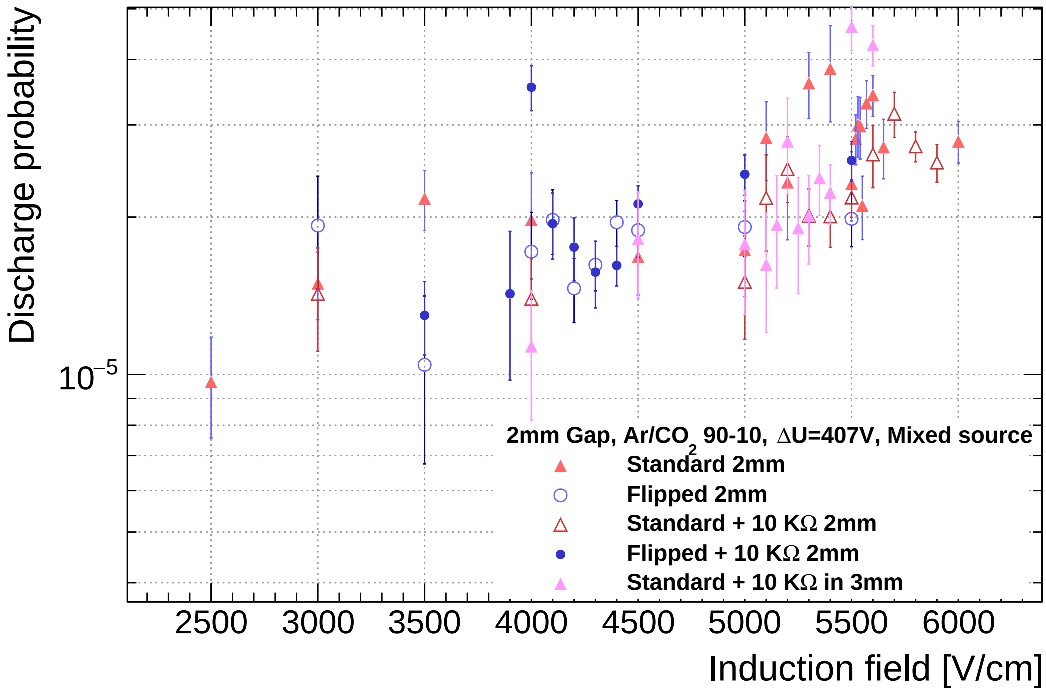

Figure 5.2: Discharge probability as a function of the applied induction field at a $\Delta U = 407\,\mathrm{V}$.

two coaxial cable capacities:

$$C_{\text{series}} = \frac{C_1 \cdot C_2}{C_1 + C_2} \tag{5.3}$$

With $\mathrm{C_{GEM}} \sim 5\,\mathrm{nF}$ and the capacities of both coaxial cables, C_{comb} is determined to $\sim 51.7\,\mathrm{pF}$. With the estimated values for L and C_{comb}, a T of $149.8\,\mathrm{ns}$ can be calculated with Eq. 5.2. The calculated solution differs by about a factor three from the measured value. However, influences of the power supply and other elements of the powering scheme are not considered in this estimation. This could lead to the conclusion, that the oscillations are an effect of the electric circuit.

5.2 Secondary discharges

Initial discharges seem to be influenced by the components of the HV scheme and can be followed by a secondary discharge. Figure 5.4 depicts the signal of a initial discharge, which is followed by a secondary. The initial discharges appears on the left and declines exponentially with oscillations. Secondary discharges are characterized

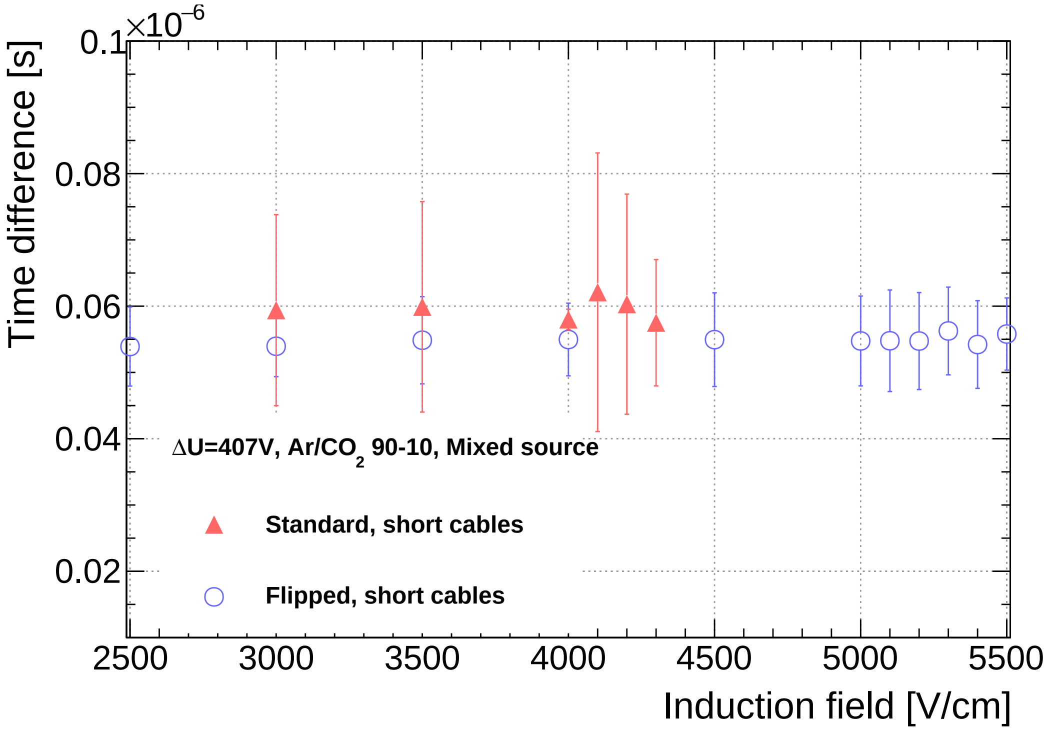

Figure 5.3: Time differences between the oscillations spikes in an initial discharge as a function of the induction field. Short coax cables with a capacity of $\sim 105\,\text{pF}$ were used.

by a larger amplitude than the initial ones and they occur after a time delay. The influence of various HV configurations on secondary discharges and their features for a wide range of induction fields has been investigated.

5.2.1 Probability for a second discharge

Figure 5.5 shows the probability for a secondary discharge for different HV configurations as a function of the induction field strength. The HV configurations were discussed in Sec 3.1.2. The discrimination between initial and secondary discharges was executed in ROOT. The signal is averaged and local extrema are recognized as described in Sec. 5.2.1. The amplitude of the first minimum is marked as the initial discharges amplitude, while the largest minima is related to the amplitude of the secondary discharge. When the absolute value of the amplitude of the secondary discharge is higher than the absolute value of the amplitude of the initial discharge and, additionally, exceeds a user-given threshold, the event is assumed to be a secondary discharge. This method has proven to reliably identify secondary discharges.

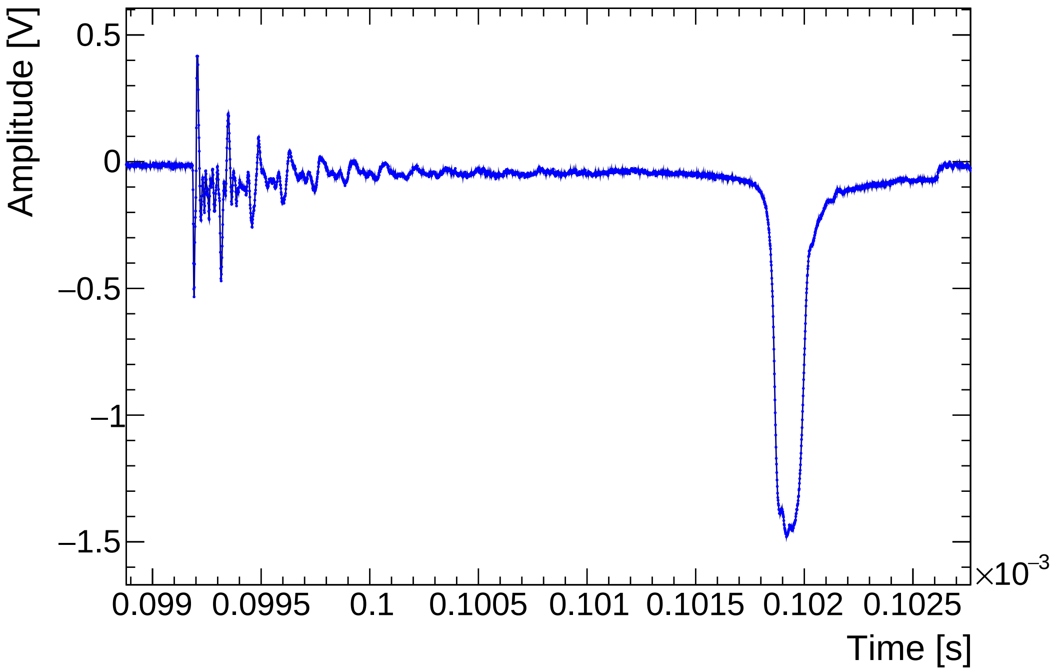

Figure 5.4: Pulse shape of a initial discharge with a secondary following on the right.

Common to all configurations is a sudden increase of the probability for a secondary discharge from zero to one at a certain field strength. For the standard configuration, the secondary discharges start to occur at a induction field strength of $5.5\,\mathrm{kV\,cm^{-1}}$. When a discharge occurs, currents are flowing between the GEM electrodes. In the standard configuration, the loading resistor is connected in series to the upper side of the GEM. Therefore, the voltage drop over the loading resistor leads to a decrease of the potential of the upper GEM electrode U_{top} until it aligns with the potential of the lower GEM electrode U_{bot}, which interrupts the discharge. This leaves the induction field strength unchanged. However, in the flipped configuration secondary discharges appear earlier at $4.3\,\mathrm{kV\,cm^{-1}}$. In this configuration, the loading resistor is connected to the lower GEM electrode. In case of a discharge, the voltage drop over the loading resistor leads to a rise of the potential of the lower GEM electrode U_{bot} until it aligns with U_{top}. As a consequence, the induction field strength rises and thus, also the probability for the occurrence of a secondary discharge.
To further investigate this shift, a second loading resistor with a resistance of $10\,\mathrm{k\Omega}$ has been connected to the GEM electrode, which was in the previous configuration directly connected to the power supply. This also decouples the capacity of the cable

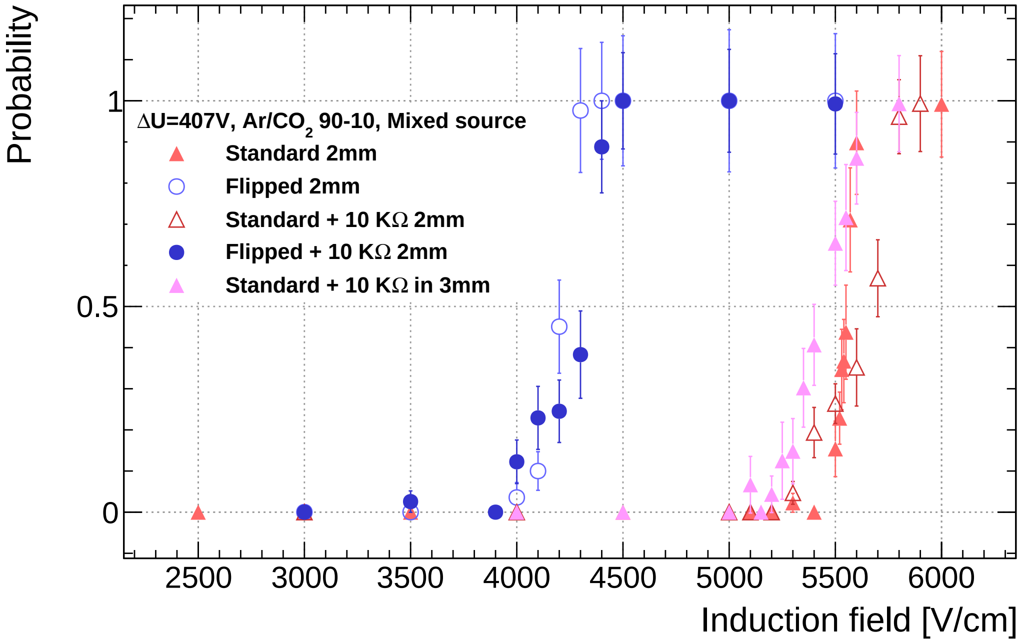

Figure 5.5: Probability for a second discharge for various configurations as a function of the induction field strength.

from the GEM. The curves with the second loading resistor are almost compatible with the curves without one, but they differ by a slight smooth out. A thorough conclusion is hard to make due to the limited statistics.
Afterwards, the induction gap for the standard configuration with a second loading resistor has been varied from 2 mm to 3 mm in order to weaken the expected rise of the induction field. However, the curve is also almost compatible with the curve for a 2 mm induction gap in standard configuration.

5.2.2 Time delay between initial and secondary discharges

In order to further investigate the origin of the secondary discharges, the time delay between the initial and the secondary discharge has been determined. First, signals of the same configuration are analyzed as depicted in Sec. 5.1.2. In case of a secondary discharge, the time values of the first signal of the initial and the secondary discharge are extracted. The time differences are collected in a histogram and fitted with a Gaussian. Figure 5.6 shows the Δt as a function of the induction field for various configurations as discussed in Sec. 3.1.2. Points with no uncertainty bars stem from data with only one secondary discharge. For a better visibility, a fraction of the data

points has been shifted by 10 V on the horizontal axis. While a trend towards faster propagations for higher induction fields in the flipped configurations is visible, the measurement points for the standard configurations are highly fluctuating.
This trend hints, that the origin of the secondary discharges might be linked to the streamer mechanism, as discussed in Sec. 1.4.2. When a discharge occurs, some of the charge flowing in the conductive link between the GEM electrodes is distributed into the detector gas. The formation of a streamer by this charge in combination with the altered induction field due to the initial discharge is rather unlikely, as the field strength is only in the order of $\mathrm{kV\,cm^{-1}}$, which is not sufficient. However, the transient behaviour of the power supply is not known, as well as the resulting change of the field. The hypothesis that secondary discharges are streamers induced by photons, which are stemming from the initial discharge, can be discarded by the fact, that the propagation time is in the order of microseconds. Photons spread with the speed of light and thus, the delay of secondary discharges should be negligible. However, the time difference between initial and secondary discharges reduces with a rising induction field strength. Stronger electric fields accelerate the charge separation and therefore the formation of a streamer. Nevertheless, the origin of the secondary discharge is still unclear and requires further investigation.

5.3 Influence of the parasitic capacity of the HV system

As the signal features of the initial discharges are influenced by the electrical properties of the HV scheme the amplitude of the secondary discharge might be as well. Of particular interest is the influence of additional parasitic capacity in the HV system. Therefore, the amplitude of the discharges has been studied while varying the cable length at an induction field strength of $5.59\,\mathrm{kV\,cm^{-1}}$. The amplitude is determined as described in 5.2.1. The values in Tab. 5.1 are extracted as the mean of a Gaussian fit to the data and compare the amplitudes of initial and secondary discharges with the corresponding cable capacities. Surprisingly, the amplitudes of the initial discharges are independent of the capacity in the coaxial cable, while the amplitudes of the secondary discharges rise with a larger capacity. The energy stored in a capacitor

Table 5.1: Discharge amplitudes as a function of the cable length.

Cable length [m]	**Capacity [pF]**	**Initial discharge amplitude [V]**	**Second. discharge amplitude [V]**
1.05	105	0.36 ± 0.02	2.33 ± 0.12
2.20	220	0.34 ± 0.02	3.25 ± 0.12

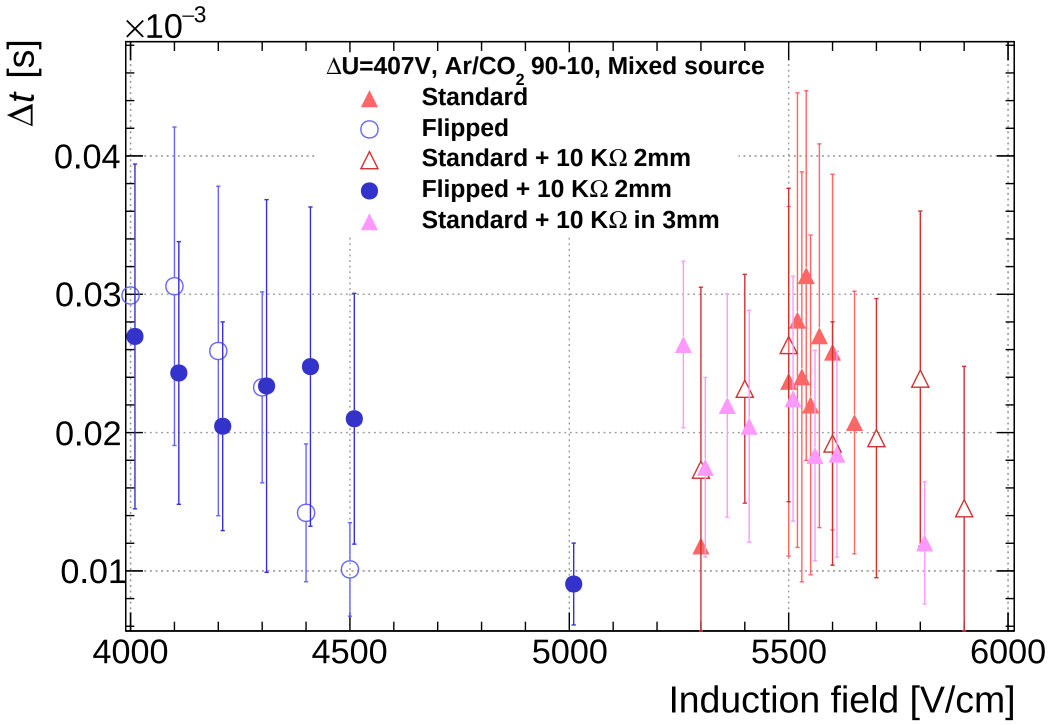

Figure 5.6: The time delay between an initial and a secondary discharge as a function of the induction field for various configurations at a $\Delta U = 407\,\mathrm{V}$ over GEM.

is given by

$$E = \frac{1}{2} \cdot C \cdot \Delta U^2 \tag{5.4}$$

The energy is directly proportional to the capacity, which in return is directly proportional to the length of the cable. Thus, it can be assumed, that the energy stored in the capacity is released in the second discharge.
Therefore, the use of a decoupling resistor is mandatory in order to prevent damage to the readout anode by high energetic secondary discharges.

Chapter 6

Summary & Outlook

6.1 Summary

The ALICE TPC upgrade has set the framework for this thesis. The prevention of discharges in the amplification region of GEMs is crucial for a stable and continuous operation of the detector. However, also secondary discharges have been observed at high induction fields and in particular this kind of discharges poses a danger to the detector and readout electronics due their high energy release. Initial and secondary discharges have been thoroughly investigated by varying detector parameters, like induction gap and field and the HV configuration. In order to automate the data acquisition and processing, a dedicated LabVIEW software has been developed for current measurements and storing pulses. To characterize the detector, energy resolution, gain and discharge probability have been determined. The latter showed no significant dependency on the induction field and the probability yields values of $\mathcal{O}(10^{-5})$ per incoming alpha particle. A thorough analysis of the pulse shape of the initial discharges yielded, that the oscillating pulse shapes seem to be shaped by the setup's electronic components. The probability for a secondary discharge has been determined for various HV configurations for 2 mm and 3 mm induction gaps over a wide range of induction fields. Secondary discharges appear at a critical value of the induction field strength and are highly dependent on the HV configuration. The delay time between initial and secondary discharges reduces with a rising induction field strength and depicts a hint at the streamer mechanism, as the formation of the latter accelerates with rising electric fields. However, no clear conclusion could be made. Therefore, the origin of secondary discharges requires further investigation. The amplitudes of secondary discharges have shown a dependency on the parasitic capacity of the HV system, while the amplitudes of the initial discharges stay remain unchanged. A decoupling resistor prevents the detector from being damaged by high energetic discharges.

6.2 Outlook

At the end of this thesis, new questions arise to further understand the phenomenon of secondary discharges. The correlation of cable capacity and secondary discharge amplitude is very interesting in the light, that 80 m long coax cables will be used in the ALICE upgrade to connect the power supply with the GEMs. The expected large discharge signals can be prevented by using decoupling resistors, but the influence of the latter on the HV system requires further investigation. The recharging process of the power supply in case of a discharge is also not very clear, thus, a simulation of the whole powering scheme should be considered.
A possible approach to investigate the origin of secondary discharges is the observation of another detector gas choice or a more uniformly distributed alpha source to exclude possible streamer creation mechanisms. So far, the detection of discharges has been solely based on the readout of the electron signal on the anode. By readout out the ion signal on the cathode, further insight on the origin of the initial and secondary discharges might be expected. In order to investigate more pulse shapes at a higher rate a faster readout setup is necessary.

Acknowledgements

First of all, I would like to thank Prof. Laura Fabbietti for giving me the chance to learn about the physics of gaseous detectors and discharges in particular. She gave me the opportunity to challenge and prove myself. Furthermore, I want to thank my supervisor M. Sc. Andreas Mathis, who taught me everything, from the physics in detectors to setting up the measuring construction and working in clean rooms. His wide knowledge, strong patience and great feedback kept me motivated throughout the thesis. He lead me with farsightedness and I very much appreciate the possibility to work with him. I want to thank Dr. Piotr Gasik for his great support in the laboratory. His lecture of gaseous detectors taught me much about the theory behind detector physics. I also want to thank Dr. Martin Berger for his knowledge and help in ROOT analysis. And also thanks to Thomas Klemenz for his assistance in the laboratory. I also want to thank E18 for sharing their laboratory and clean room with me. I want to thank the people from E12 for their motivating spirit and feedback. I enjoyed the productive atmosphere. Special thanks goes to the electronic division of the Physics department. The execution of this thesis would not have been possible without their work and supply. Besides, I want to thank everyone who contributed. Finally, I want to thank my parents, my brother and my grandmother for their constant support and that they never stop believing in me.

Appendix A

Error Calculation

The energy resolution of escape and absorption peak is given by the formula:

$$ER = \frac{\frac{c_1 \cdot \sigma_1}{\mu_1} + \frac{c_2 \cdot \sigma_2}{\mu_2}}{c_1 + c_2} \tag{A.1}$$

where c_1 and c_2 are the amplitudes of the peaks, μ_1 and μ_2 are the mean values and σ_1 and σ_2 are the standard deviation. The error is then calculated to:

$$\begin{aligned} \Delta ER = \Bigg[& \left(\frac{\Delta c_1 \sigma_1}{\mu_1 (c_1 + c_2)}\right)^2 + \left(\frac{c_1 \Delta \sigma_1}{\mu_1 (c_1 + c_2)}\right)^2 + \left(\frac{c_1 \sigma_1 \Delta \mu_1}{\mu_1^2 (c_1 + c_2)}\right)^2 \\ & + \left(\frac{c_1 \sigma_1 \Delta c_1}{\mu_1 (c_1 + c_2)^2}\right)^2 + \left(\frac{c_1 \sigma_1 \Delta c_2}{\mu_1 (c_1 + c_2)^2}\right)^2 + \left(\frac{\Delta c_2 \sigma_2}{\mu_2 (c_1 + c_2)}\right)^2 \\ & + \left(\frac{c_2 \Delta \sigma_2}{\mu_2 (c_1 + c_2)}\right)^2 + \left(\frac{c_2 \sigma_2 \Delta \mu_2}{\mu_2^2 (c_1 + c_2)}\right)^2 + \left(\frac{c_2 \sigma_2 \Delta c_2}{\mu_2 (c_1 + c_2)^2}\right)^2 \\ & + \left(\frac{c_2 \sigma_2 \Delta c_1}{\mu_1 (c_1 + c_2)^2}\right)^2 \Bigg] \end{aligned} \tag{A.2}$$

Bibliography

[1] L. Cifarelli. The Quark-Gluon Plasma, a nearly perfect fluid. *Europhys. News*, 2012.

[2] ALICE Collaboration. Technical Design Report for the Upgrade of the ALICE Time Projection Chamber. 2014.

[3] J. Alme et al. The ALICE TPC, a large 3-dimensional tracking device with fast readout for ultra-high multiplicity events. 2010.

[4] GEM-TPC Collaboration. Technical Design Study for the PANDA Time Projection Chamber. 2012.

[5] G. Charpak, R. Bouclier, T. Bressani, J. Favier, and Č. Zupančič. The use of multiwire proportional counters to select and localize charged particles. 1968.

[6] Martin Berger. Development, Commissioning and Spatial Resolution Studies of a new GEM based TPC. 2015.

[7] F.V. Böhmer, M. Ball, and S. Dørheim. Space-Charge Effects in an Ungated GEM-based TPC. *ArXiv e-prints*.

[8] Pedro Bicudo, Nuno Cardoso, and Marco Cardoso. The chiral crossover, static-light and light-light meson spectra and the deconfinement crossover. *arXiv*, 2011.

[9] Bogdan Povh, Christoph Scholz, Frank Zetsche, and Klaus Rith. Teilchen und Kerne. 2014.

[10] P. Fonte and V. Peskov. On the physics and technology of gaseous particle detectors. 2009.

[11] J. Alme et al. The ALICE TPC, a large 3-dimensional tracking device with fast readout for ultra-high multiplicity events. *Nuclear Instruments and Methods in Physics Research A*, 622:316–367, October 2010.

[12] B. Abelev et al. Upgrade of the ALICE Experiment: Letter of Intent. Technical Report CERN-LHCC-2012-012. LHCC-I-022. ALICE-UG-002, CERN, Geneva, Aug 2012.

[13] F. Sauli. GEM: A new concept for electron amplification in gas detectors. *Nucl. Instr. Meth. A.*

[14] S. Bachmann et al. Charge amplification and transfer processes in the gas electron multiplier. *Nuclear Instruments and Methods in Physics Research A 438 (1999) 376-408.*

[15] F. Böhmer et al. Simulation of space-charge effects in an ungated GEM-based TPC. *NIM A 719 (2013) 101.*

[16] S. Bachmann et al. Discharge studies and prevention in the gas electron multiplier (GEM). *Nuclear Instruments and Methods in Physics Research A 479 (2002) 294-308.*

[17] H. Raether. Electron avalanches and breakdown in gases. *Butterworths.*

[18] V. Peskov and P. Fonte. Research on discharges in micropattern and small gap gaseous detectors. 2009.

[19] Stefan Weber. Discharge probability studies with GEM detectors. 2014.

[20] Piotr Gasik. Discharge studies with single- and multi-GEM structures in a scope of the ALICE TPC upgrade. 2016.

[21] ALICE Collaboration. Addendum to the Technical Design Report for the Upgrade of the ALICE Time Projection Chamber. *ALICE-TDR-016-ADD-1*, 2015.

[22] LabVIEW. `www.ni.com/labview`.

[23] Keithley 6517b. `http://www.tek.com/sites/tek.com/files/media/media/resources/6517B_DataSheet.pdf`.

[24] Tektronix MSO DPO 4104b. `http://de.tek.com/oscilloscope/mso4000-dpo4000`.

[25] Huntsman Advanced Materials GmbH. ARALDITE epoxy 2011. `www.huntsman.com`.

[26] iseg. `www.iseg-hv.com`.

[27] FAST ComTec GmbH. MCA4. `https://www.fastcomtec.com/products/mca/mca4system/`.

[28] H. Bichsel, D.E. Groom, and S.R. Klein. Passage of particles through matter. 2016.

[29] K. A. Olive et al. Review of Particle Physics. *Chin. Phys.*, C38:090001, 2014.

[30] Eckert & Ziegler. Alpha spectrometry sources. http://www.ezag.com/fileadmin/ezag/user-uploads/isotopes/isotopes/Isotrak/isotrak-pdf/Product_literature/EZN/04_section04_alpha_spectrometry_sources.pdf.